PHOTONICS Research

Broadband meta-converters for multiple Laguerre-Gaussian modes

Huade Mao,[1,†] Yu-Xuan Ren,[2,†] Yue Yu,[3,†] Zejie Yu,[3] Xiankai Sun,[3,6] Shuang Zhang,[1,4] and Kenneth K. Y. Wong[1,5,*]

[1]Department of Electrical and Electronic Engineering, The University of Hong Kong, Hong Kong, China
[2]Institute for Translational Brain Research, Shanghai Medical School, Fudan University, Shanghai 200032, China
[3]Department of Electronic Engineering, The Chinese University of Hong Kong, Hong Kong, China
[4]Department of Physics, The University of Hong Kong, Hong Kong, China
[5]Advanced Biomedical Instrumentation Centre, Hong Kong Science Park, Hong Kong, China
[6]e-mail: xksun@cuhk.edu.hk
*Corresponding author: kywong@eee.hku.hk

Received 22 February 2021; revised 8 June 2021; accepted 23 June 2021; posted 28 June 2021 (Doc. ID 423344); published 11 August 2021

Metasurface provides miniaturized devices for integrated optics. Here, we design and realize a meta-converter to transform a plane-wave beam into multiple Laguerre-Gaussian (LG) modes of different orders at various diffraction angles. The metasurface is fabricated with Au nano-antennas, which vary in length and orientation angle for modulation of both the phase and the amplitude of a scattered wave, on a silica substrate. Our error analysis suggests that the metasurface design is robust over a 400 nm wavelength range. This work presents the manipulation of LG beams through controlling both radial and azimuthal orders, which paves the way in expanding the communication channels by one more dimension (i.e., radial order) and demultiplexing different modes.

https://doi.org/10.1364/PRJ.423344

1. INTRODUCTION

The Laguerre-Gaussian (LG) mode, a solution of the Helmholtz equation in cylindrical coordinates, characterized by the radial index [1], p, and the azimuthal index [2], l, has attracted tremendous attention recently owing to the ability to encode information [3–6]. The azimuthal index, known as the orbital angular momentum (OAM) [2], has shown applications in object detection [7,8], optical communication [9], holography imaging [10], etc., mainly counting on the momentum conservation during propagation [11]. Meanwhile, the LG mode, as a complete orthogonal basis [7], has been demonstrated to increase the communication speed [12,13], e.g., multiplexing and demultiplexing in multiple orthogonal OAM channels [13]. However, the radial index has been largely underexplored by the community as it is not supported by the single-mode fiber used in many optical setups. However, this is not a concern in the free space. Since the radial index is a valid quantum number [14] and could be transmitted through a graded-index fiber [1] or in free space, it has the potential to further increase the capacity of communication system [1] by one more dimension (i.e., radial order).

However, many studies primarily focused on the generation [3,6,15] or the observation [16,17] of LG modes. For example, a mode sorter [4] was proposed to generate up to 325 LG modes by utilizing seven phase masks to transform an array of Gaussian beams into the quasi-complete set of LG mode beams. Despite its technical brilliance, it still transforms each Gaussian beam into a single LG mode but not multiple ones, not to mention the setup's complexity.

Here, we report a complex-modulated metasurface to simultaneously tailor multiple LG modes. Many previous optical devices for LG modes generation [4,6,18] feature phase-only modulation, which need an iterative algorithm [19] to minimize the error between the output and target field. In recent years, complex modulation [20,21] was proposed to generate LG modes. However, they were only able to generate one LG mode at a time. By comparison, our metasurface could (1) generate the field in a faster way (no need for iteration) and (2) achieve more sophisticated goals (simultaneous conversion and demultiplexing for multiple LG modes). Our metasurface consists of a 2D array of Au nano-antennas on a glass substrate coated with indium tin oxide. Our experiments suggest that the designed metasurface performs in a broadband wavelength spanning over 400 nm, which is also corroborated by simulation. As the metasurface is a promising miniaturization technique [22–25] and many high-order LG modes are achieved through a single chip [6,26], our work paves the way to future LG modes application and communication channel expansion.

2. COMPLEX MODULATION

The building block of the metasurface is the nano-antenna made of Au [Fig. 1(a)], with the height h and width w_x fixed respectively at 80 nm and 200 nm throughout the paper. The orientation of the nano-antenna ("atom") defines the Pancharatnam–Berry phase modulation [27–30].

When a left-handed circularly polarized (LCP) light impinges onto this unit, the Au block, functioning as a locally defined birefringent crystal, could alter the amplitude and phase for the orthogonally decomposed light respectively along the fast axis and slow axis, thus transforming a certain amount of LCP into right-handed circular polarized (RCP) light [28,31]. The RCP component [32] from transmitted light is

$$S_{\text{out}} = \langle R|\Gamma(-\alpha)\hat{Q}\Gamma(\alpha)|L\rangle, \tag{1}$$

where R and L denote RCP and LCP, respectively; $\Gamma(\alpha)$ is the rotation matrix; α is the orientation angle of the block in Fig. 1(a); and $\hat{Q}$ is the transformation matrix.

We perform finite-difference time-domain (FDTD) simulation to calculate the full field of the transmitted RCP light through nano-blocks with various orientations and geometries (Appendix A). We select 10 different configurations with length ranging from 220 nm to 400 nm while keeping the period P of the unit as 500 nm, and orientation from 0 to π to encode the full phase and amplitude of the light wave. In order to offset dynamic phase's difference, each configuration has a unique initial orientation angle as shown in the red block [Fig. 1(b) and Appendix A]. The performance of 10 configurations was evaluated in the wavelength range from 500 to 1500 nm using FDTD simulation. The complete conversion maps of both the amplitude and phase are revealed in Figs. 1(c) and 1(d).

The laser beam is converted to LCP before shining on the metasurface under test [Fig. 1(e)]. The RCP component of the forward scattering light will carry the information encoded with multiple LG modes deflected into different angles (demultiplexing).

3. METASURFACE FIELD

The electric field of a certain Laguerre-Gaussian beam can be written as [33]

$$\mathrm{LG}_p^l = \frac{\sqrt{2}r^{|l|}}{w_0^{|l|+1}} \cdot \exp\left(-\frac{r^2}{w_0^2}\right) \cdot \mathrm{LP}_p^{|l|}\left(\frac{2r^2}{w_0^2}\right) \cdot \exp(il\phi), \tag{2}$$

where p is the radial index; l is the azimuthal index that represents the magnitude of OAM; r and ϕ are the cylindrical coordinates; w_0 is the beam waist; and LP is the Laguerre polynomial. In the past, devices featuring only phase modulation, whether a metasurface [6] or diffraction filter [18], have been proposed for generating LG modes. However, for more than two LG modes' encoding, phase-only modulation could not achieve zero-error (Appendix B). Complex modulation [20,21], proposed in recent years, has not been explored in multiple LG modes encoding.

Here, we show that an incident plane-wave beam can be converted into multiple LG modes diffracted into arbitrary directions in transmission by a metasurface, whose complex modulation is expressed as

$$M = \sum_s \sigma_s (\mathrm{LG}_p^l)_s \cdot \exp(i \cdot \sin\theta \cdot \vec{g_s} \cdot \vec{\rho}) = A_M \exp(i\phi_M), \tag{3}$$

where σ_s represents different weight assigned to the specified LG mode; LG_p^l denotes the normalized complex distribution of each mode; and θ is the deflection angle while g_s and ρ are the deflection direction and pixel vector, respectively [inset of Fig. 1(e)]. The pixel vector $\vec{\rho}$ points from the center point to one pixel on the metasurface. The amplitude and phase parts

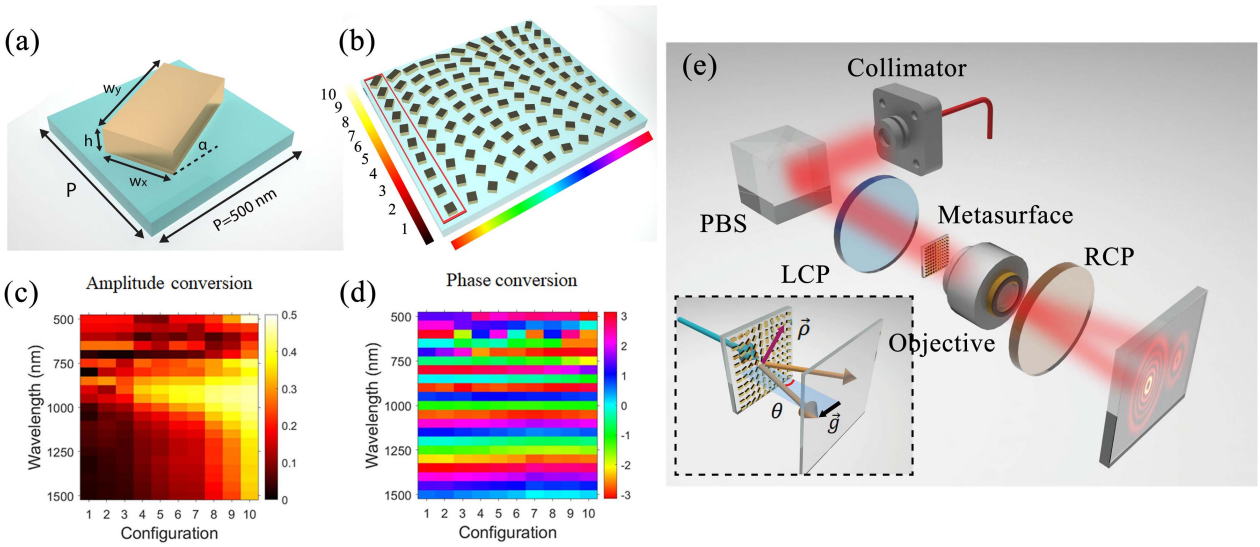

Fig. 1. (a) Configuration of a unit block. P, period; w_x, width; w_y, length; h, height; α, orientation angle. (b) Configurations of Au block to accomplish complex modulation. The color bars are amplitude range of [0, 0.5] and phase range of $[-\pi, \pi]$, which are the same as in (c) and (d). (c), (d) Amplitude and phase conversion over 500–1500 nm range for the 10 configurations specified in the red rectangle in (b). (e) Experimental setup. PBS, polarization beam splitter; LCP, LCP generator, consisting of a polarizer and a $\lambda/4$ wave plate; RCP, RCP filter, composed of a polarizer and a $\lambda/4$ wave plate.

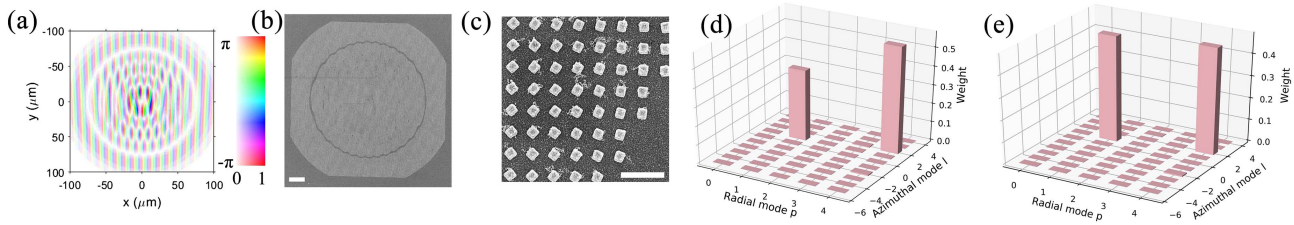

Fig. 2. (a) Rounded complex pattern to convert the fundamental Gaussian beam into a combination of LG_4^2 and LG_1^1 directed to $\vec{g}_1 = (1,0)$, with angles $\theta = 5^\circ$ and $\theta = 10^\circ$. The assigned weight has a ratio of $LG_4^2 : LG_1^1 = 6:4$. (b) Overall scanning electron microscope (SEM) image. (c) Zoomed SEM image. (d) LG decomposition results for the complex pattern in (a) without deflection. (e) LG decomposition results for the modes combination of $LG_4^2 : LG_1^1 = 1:1$. Scale bar: 20 μm in (b); 1 μm in (c).

of the output field in Eq. (3) could be achieved by the metasurface with complex modulation which is fabricated by electron-beam lithography.

The meta-convertor allocates the incident light energy into different decomposition modes according to the designed information magnitude. As an example, we convert the plane-wave beam into two LG modes with non-identical deflection angles. Figure 2(a) shows the complex modulation of the combination of LG_4^2 and LG_1^1 modes with their deflection direction being respectively $\overrightarrow{g_1} = (1,0)$ and $\overrightarrow{g_2} = (1,0)$, with deflection angles θ of 5° and 10°, and an amplitude ratio of 6:4. We fabricate the metasurface by a mapping from the complex field [Fig. 2(a)] to the exact configuration in Fig. 1(b). Figure 2(b) shows the scanning electron microscope image of the fabricated metasurface with a zoom-in view shown in Fig. 2(c), which elaborates the building blocks of various angles. The metasurface is composed of 400 × 400 unit blocks. Since each unit block has a size of 500 nm × 500 nm, the metasurface has an area of 200 μm × 200 μm.

We decompose the complex pattern to determine the coefficient for each mode as (Appendix C)

$$C_p^l = \frac{\left\langle LG_p^l, U \right\rangle}{\left\langle LG_p^l, LG_p^l \right\rangle}, \tag{4}$$

where U denotes the complex field without deflection to maintain central symmetry and the denominator is the normalization term. This process is one kind of Fourier decomposition with the Fourier basis being the LG modes which form the complete set [34]. The result [Fig. 2(d)] suggests a ratio of 6:4 between the modes of LG_4^2 and LG_1^1, which is well consistent with our design.

Here, we analyzed the effect of fabrication error, detailed in Section 4. Under our assumption, ±10 nm deviation of width and length of the Au block will cause an average error of mostly lower than 10%, which is acceptable. Then, we also evaluate the influence of fabrication error on the decomposition results (Appendix C). The decomposition would have no significant change provided that the fabrication error has a mean of 0. The decomposition error deviates only 4.5% for a mean of 0.05, which suggests the robust tolerance to the fabrication error. This has also been validated with another design [Fig. 2(e)] with a combination of $LG_4^2 : LG_1^1 = 1:1$.

4. ERROR ANALYSIS

The tolerance of the size of the nano-block is critical for the broadband performance. The metasurface is fabricated with the electron-beam lithography. But there is no statistical data reflecting the fabrication error for our metasurface. Empirically, the fabrication has an error of 10 nm. So here we assume the machine will have a 10 nm deviation on both the width and length of the Au block and the deviation is Gaussian distributed. Therefore, the probability density function of the distribution could be represented as follows:

$$p(Z;\mu,\Sigma) = \frac{1}{(2\pi)^{\frac{d_i}{2}}|\Sigma|^{\frac{1}{2}}} \cdot \exp\left[-\frac{1}{2}(Z-\mu)^T\Sigma^{-1}(Z-\mu)\right], \tag{5}$$

where $Z = (w_x, w_y)^T$ is the vector of the length and width of the Au block; $\mu = (\mu_x, \mu_y)^T$ is the mean of the length and width; $\Sigma = (\sigma_1^2 \quad 0; 0 \quad \sigma_2^2)$ is the covariance matrix of the Gaussian distribution, where two variables are uncorrelated under our assumption; and d_i denotes the dimension of the variable.

The total possible range of Z here, in our consideration, is [190,210] nm for width and $[\mu_y - 10, \mu_y + 10]$ nm for length. We conduct full-wave FDTD simulation over this region, and get the error map:

$$\epsilon(Z) = \frac{|C(w_x, w_y; \alpha_0) - C(\mu_x, \mu_y; \alpha_0)|}{0.464}, \tag{6}$$

where $C(x, y; \alpha)$ denotes the complex modulation under the configuration x and y given orientation α.

The average error ξ could be calculated as

$$\xi = \int_{\mu_x-10}^{\mu_x+10}\int_{\mu_y-10}^{\mu_y+10} \epsilon(Z) \cdot p(Z;\mu,\Sigma)\mathrm{d}w_x\mathrm{d}w_y, \tag{7}$$

where the integral region is the total possible range of Z.

Since the two variables, width w_x and length w_y are uncorrelated, we just draw one variable at a time in Fig. 3. If the standard deviation σ_i $(i = 1, 2)$ is small enough, the most distribution will be inside our consideration region. Here we assign three levels to different standard deviations, ranging from "pessimistic," "neutral," to "optimistic" in Fig. 3 and Table 1. When the standard deviation σ is set to 3.33 nm, nearly 99.4% of the whole distribution, which is the yellow area in Fig. 3, is within our consideration region. When the standard deviation σ goes up to 10 nm, only 46.5% of the distribution falls into

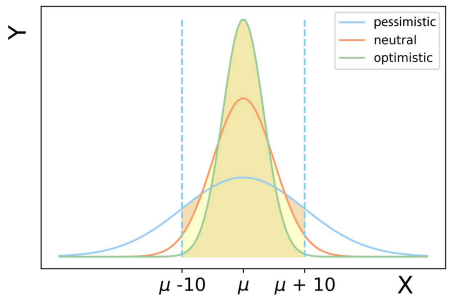

Fig. 3. Gaussian distribution under three scenarios: "pessimistic," "neutral," "optimistic."

Table 1. Three Scenarios of Gaussian Distribution

Std	Coverage	Level
$\sigma_1 = \sigma_2 = 10$	46.5%	Pessimistic
$\sigma_1 = \sigma_2 = 5$	91.0%	Neutral
$\sigma_1 = \sigma_2 = 3.33$	99.4%	Optimistic

our assumption region, which is termed "pessimistic" in this case. We will calculate the total error according to Eq. (7) under these three scenarios.

The error map is revealed in Fig. 4 for four nano-block configurations. The first and third columns, captioned "Error" in the figure, are the absolute error among the fabrication regions. The second and fourth columns show the error with Gaussian distribution under "optimistic" assumption.

The average error ξ, elaborated in Eq. (7), is calculated under all the three scenarios and listed in Table 2. Even under pessimistic assumption, the average error is about or lower than 10%, which is acceptable. And in Appendix C, we will see that the deviation will be fully waived under LG mode decomposition, which shows the robustness of our design.

5. SIMULATION AND EXPERIMENTS

The holographic image of the metasurface could be calculated through a complex transmission function [32,35],

$$H(x,y) = \sum_{m,n} M_{mn} \cdot \frac{\exp[ikR_{mn}(x,y)]}{R_{mn}(x,y)}, \tag{8}$$

where M_{mn} represents a pixel on the metasurface determined by Eq. (8); k is the wavenumber; $R_{mn}(x,y)$ denotes the distance between M_{mn} and the position (x,y) on the holographic image H. The final normalized intensity is calculated as $I_{\text{norm}} = \langle H,H\rangle / \langle H,H\rangle_{\max}$.

We next evaluate the broadband performance of the metasurface. The complex pattern M_{mn} of a certain wavelength is converted using the broadband conversion map for 10 configurations [Figs. 1(c) and 1(d)]. The metasurfaces are designed at the wavelength of 1000 nm. The complex pattern varies slightly from 500 nm to 1500 nm (Visualization 1). Then we alter the wavenumber k in Eq. (8) to simulate the holographic image.

The supplementary visualization shows how the complex pattern and the LG decomposition results change over the broadband wavelength range. Visualization 1 is about the metasurface featuring modes of $\text{LG}_4^2 : \text{LG}_1^1 = 6:4$. In the video, the first row contains the amplitude and phase map of the complex field without deflection over the wavelength range from 500 nm to 1500 nm. The third figure of the first row is the bar chart of the LG decomposition results. The second row contains the complex field of the metasurface with deflection, which is the fabricated complex field we use for experiments.

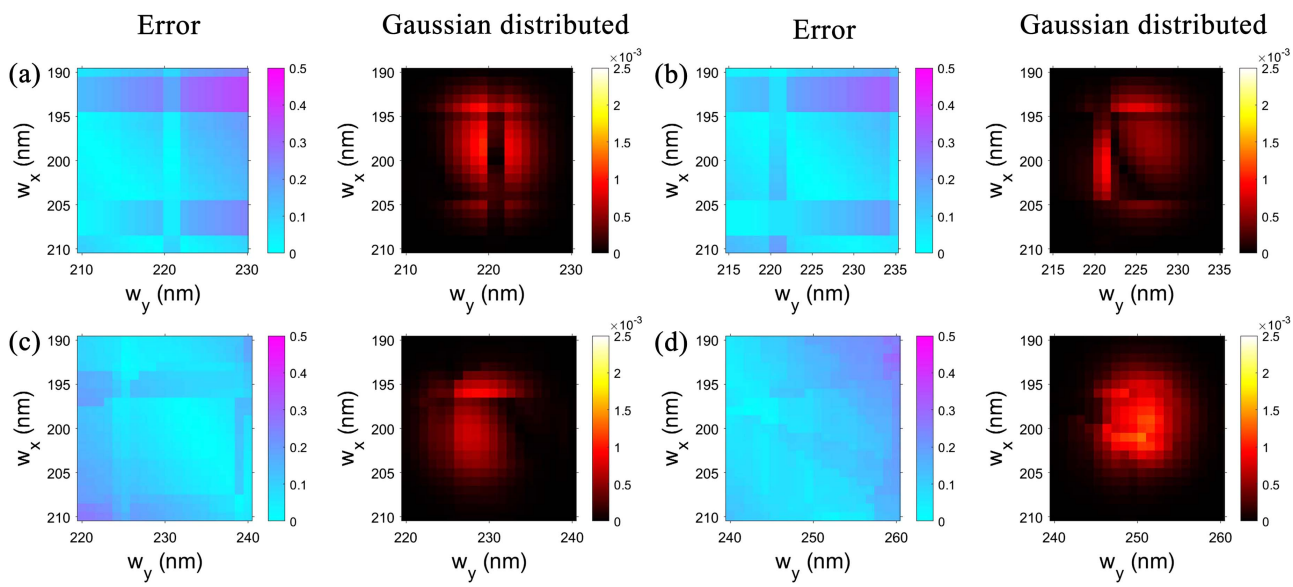

Fig. 4. Error distribution for four different configurations with 10 nm deviation along the width and length of the Au block. The first and third columns are the absolute error over different width and length. The second and fourth columns are the Gaussian-distributed error from the desired configuration. For the four configurations we selected here, the width w_x is fixed at 200 nm. The lengths w_y are (a) 220 nm, (b) 225 nm, (c) 230 nm, and (d) 250 nm.

Table 2. Parameters Approximation[a]

η_N	0	0.1	0.2	0.3	0.4	0.5	0.6	0.7	0.8	0.9	1.0
η_P	0	0.0464	0.0928	0.1392	0.1856	0.2320	0.2784	0.3248	0.3712	0.4176	0.4640
w_y (nm)	0	220	225	230	250	255	265	270	300	330	400
α_0	0	0	0	$-\frac{1}{60}\pi$	$-\frac{1}{18}\pi$	$-\frac{1}{12}\pi$	$-\frac{1}{9}\pi$	$-\frac{5}{36}\pi$	$-\frac{1}{6}\pi$	$-\frac{7}{36}\pi$	$-\frac{41}{180}\pi$
η_{ac}	0	0.0452	0.103	0.125	0.181	0.236	0.275	0.326	0.378	0.424	0.450
ϕ_{ac}	0	−1.129	−1.112	−1.177	−1.080	−1.154	−1.208	−1.212	−1.151	−1.112	−1.100
ξ	0	0.258%	2.23%	3.39%	2.17%	1.53%	4.77%	5.82%	2.30%	2.07%	2.90%
ξ_1	0	11.17%	9.29%	8.47%	10.68%	8.39%	9.85%	8.20%	8.62%	6.83%	5.18%
ξ_2	0	9.48%	7.87%	7.28%	9.95%	6.91%	9.01%	7.00%	7.92%	6.30%	4.50%
ξ_3	0	7.49%	6.04%	6.10%	9.38%	5.58%	8.23%	5.89%	7.19%	5.75%	3.96%

[a]η_N: desired quasi-amplitude conversion. η_P: desired actual amplitude conversion. w_y: length of the nano-antenna along the y axis. α_0: initial orientation angle. Given the predetermined length w_y and orientation α_0, the actual amplitude and phase conversion are denoted as η_{ac} and ϕ_{ac}. ξ: error between the actual and desired complex conversion. Error under three different Gaussian distributions: ξ_1: pessimistic; ξ_2: neutral; ξ_3: optimistic.

Experimentally, the performance of the fabricated metasurface is evaluated at various wavelengths (1030 nm, 1200 nm, and 808 nm) to demonstrate the broadband modulation ability. The diffractive images are collected at a distance of 1.5 mm or 2.0 mm from the metasurface (Fig. 5). Figure 5(a) shows the diffraction pattern for $\lambda = 1030$ nm. The LG_4^2 and LG_1^1 deflect to roughly 130 μm and 260 μm at a propagation distance of 1.5 mm, which correspond to the diffraction angles of 5° and 10°, respectively. As seen from both the hologram simulation and the experiment [Fig. 5(a)], there are apparent interference fringes in the region where the two LG modes overlap, which is owing to the insufficient separation in the near field. However, the fringes will disappear when the paired beams propagate further (2 mm away from the metasurface), as shown in Fig. 5(b).

In Figs. 5(c) and 5(d), we test the performance of the meta-converter at two other wavelengths of 1200 nm and 808 nm, and the experiments (bottom) agree well with the simulation results (top). We analyze its error and efficiency from 700 nm to 1500 nm [Fig. 5(e)] through simulation. The decomposition error measures the deviation of energy allocation from design and the efficiency measures the ratio of energy flowing into desired modes defined in Eq. (C10). Take the metasurface in Fig. 2(b) for example. The amplitude ratio of the desired modes is $LG_4^2 : LG_1^1 = 6:4$. After normalization, the desired

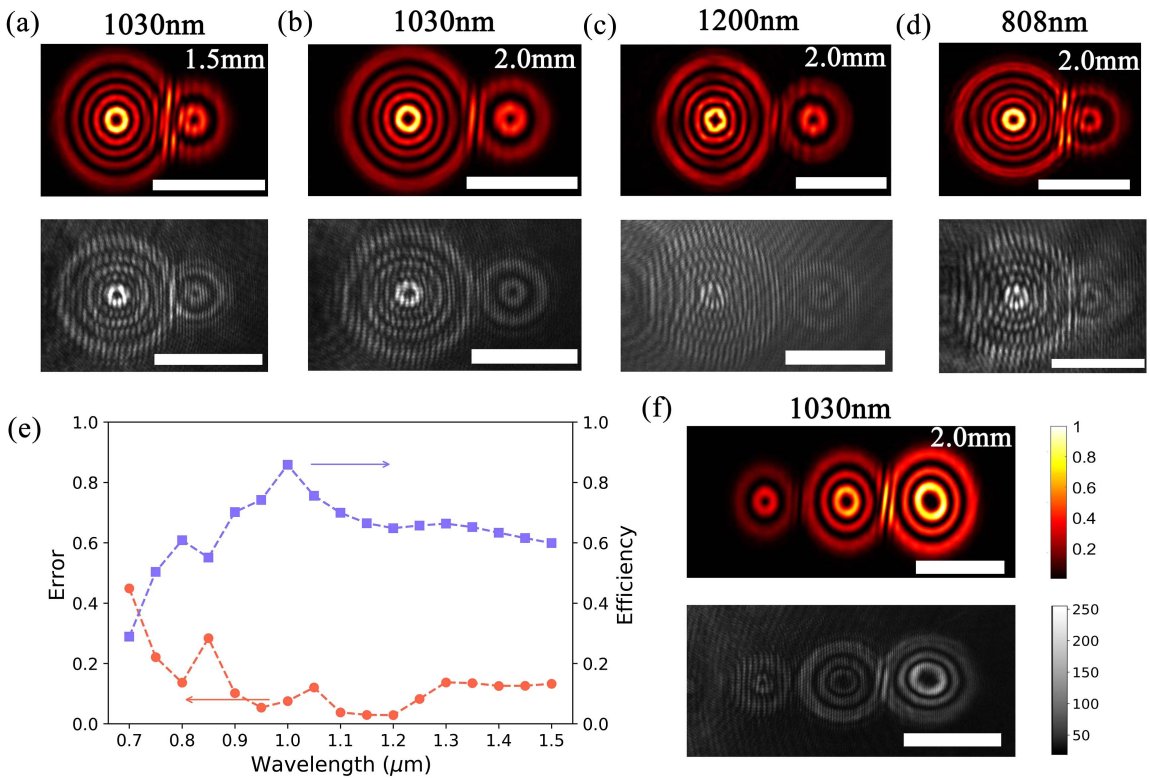

Fig. 5. Experimental results: broadband performance of meta-converters. (a)–(d) Diffraction patterns with metasurface designed for $LG_4^2 : LG_1^1 = 6:4$. The test wavelength and the measurement distance from the metasurface are all labeled with the beam profile. First row: simulation. Second row: experiments. (e) Simulated broadband performance for the meta-converter of $LG_4^2 : LG_1^1 = 6:4$ in terms of error and efficiency. (f) Metasurface contains modes of $LG_1^1 : LG_2^2 : LG_2^3 = 3:4:5$. The left edge corresponds to zero deflection for all figures. Scale bar for all: 200 μm.

coefficients vector is $\vec{\omega} = (0.6,0.4)$. After decomposition at 1 μm, the decomposed vector is $\vec{\sigma} = (0.504,0.354)$. The error is calculated as 0.076 and the efficiency is 0.858, which are both acceptable. We repeat the procedure from 700 to 1500 nm with a step of 50 nm to get Fig. 5(e). It shows that from 800 nm and up to 1500 nm, the metasurface has an error about or below 10% mostly (except 28% at 850 nm). Although the above analysis adopts two LG modes, in general, the design and analysis procedure could apply to a combination of multiple LG modes. For demonstration, we show the three LG modes encoding with an energy ratio of $LG_1^1 : LG_2^2 : LG_2^3 = 3:4:5$. Since the RCP filter is not at 100% efficiency, the unconverted LCP passing the metasurface will form an interference pattern resembling its arrangement, which will cause a concentric ring interference at the center in Figs. 5(a)–5(d).

Although the result is decent for three LG modes here, the metasurface has an issue of energy transmission efficiency. The maximum amplitude modulation is 0.464. The transmitted power is 21.5% at most. Given the metasurface is complex modulated, the whole energy transmission would be even lower. If we increase the amount of LG modes, there must exist a limit where the energy allocated to each mode is undetectable in experiment. Future work about dielectric metasurface to improve the energy transmission is prospected.

6. CONCLUSION

In conclusion, we designed a metal metasurface to generate multiple LG modes and separate them simultaneously. The metasurface features a complex modulation and has a decent performance over the 400 nm wavelength range. Although we demonstrate the energy allocation into a limited number of LG modes, the meta-convertor could in principle distribute the light energy into an arbitrary number of modes. Since the radial index of the LG mode could be transmitted through a graded-index fiber [1,36] or in free space, it is envisaged it could potentially increase the communication bandwidth in the optical communication systems with integrated optical devices.

APPENDIX A: COMPLEX MODULATION

We set two basic orthogonal electric field units as

$$E_x = \vec{e_x} \cdot \exp[i(kz - \omega t)], \tag{A1}$$

$$E_y = \vec{e_y} \cdot \exp[i(kz - \omega t)], \tag{A2}$$

where k denotes the wave vector, z is the propagation distance along the z axis, ω is the radius frequency, and t is the time.

Then the light field could be written in Jones vector form:

$$|x\rangle = \begin{bmatrix} 1 \\ 0 \end{bmatrix}, \tag{A3}$$

$$|y\rangle = \begin{bmatrix} 0 \\ 1 \end{bmatrix}, \tag{A4}$$

where $|x\rangle$ and $|y\rangle$ denote the polarized field along the x axis and y axis, respectively.

As LCP and RCP could be decomposed into two linear polarization, and LCP and RCP could be written as follows:

$$|L\rangle = \frac{1}{\sqrt{2}} \begin{bmatrix} 1 \\ i \end{bmatrix}, \tag{A5}$$

$$|R\rangle = \frac{1}{\sqrt{2}} \begin{bmatrix} 1 \\ -i \end{bmatrix}, \tag{A6}$$

where $|L\rangle$ and $|R\rangle$ denote LCP and RCP carrying unit power, and i represents the $\pi/2$ phase shift between two linear polarizations.

In our metasurface, each periodic unit block contains the glass substrate and Au nano-block as in Fig. 1(a). The configuration of the Au block is determined by three parameters, namely, the width w_x, the length w_y, and the orientation angle α.

The Au nano-block, considered as a birefringent crystal, has its ordinary and extraordinary refractive index as n_o and n_e along the x and y axes given no orientation angle. If the incident light is LCP, the output field after the Au block's tuning is

$$|\Psi\rangle = R(-\alpha)\hat{Q}R(\alpha)|L\rangle, \tag{A7}$$

where

$$R(\alpha) = \begin{pmatrix} \cos\alpha & -\sin\alpha \\ \sin\alpha & \cos\alpha \end{pmatrix}, \tag{A8}$$

with α being the orientation angle of the Au block,

$$\hat{Q} = \begin{pmatrix} A_o e^{i\phi_o(z)} & 0 \\ 0 & A_e e^{i\phi_e(z)} \end{pmatrix}, \tag{A9}$$

where A_o and A_e denote the transmission coefficient along the ordinary and extraordinary direction, respectively, while $\phi_o(z)$ and $\phi_e(z)$ represent the phase modulation resulting from the birefringence.

In the end, we shall extract the RCP component of the output field $|\Psi(z)\rangle$ [32], which is

$$\begin{aligned} E_{\text{out}} &= \langle R|\Psi(z)\rangle = \frac{1}{\sqrt{2}}(1 \quad -i)^* \cdot |\Psi(z)\rangle \\ &= i \cdot \sin\left[\frac{kd(n_o - n_e)}{2}\right] e^{i\left[\frac{kd(n_o+n_e)}{2} + 2\alpha\right]}, \end{aligned} \tag{A10}$$

where d is the height of our proposed Au block.

From above, we could have the output field specially modulated in amplitude and phase as

$$A_{\text{out}} = \text{abs}(E_{\text{out}}) = \sin\left[\frac{kd(n_o - n_e)}{2}\right], \tag{A11}$$

$$\phi_{\text{out}} = \text{angle}(E_{\text{out}}) = \frac{kd(n_o + n_e)}{2} + 2\alpha + \frac{\pi}{2}. \tag{A12}$$

In phase modulation, the dynamic phase $kd(n_o + n_e)/2$ is determined by the Au block's own parameter, and the Pancharatnam–Berry phase 2α is dependent on the orientation angle, which means if the Au block is rotated from 0 to π, the output phase could have a 0–2π modulation range, which is consistent with the phase conversion in Fig. 6(b).

The FDTD simulation results are presented in Figs. 6(a) and 6(b). We set the width w_x and height h to 200 nm and 80 nm, respectively, and alter the length w_y from 200 to 400 nm. Such a range could reach the maximum amplitude conversion range, e.g., from 0 to 0.464, and is within our fab-

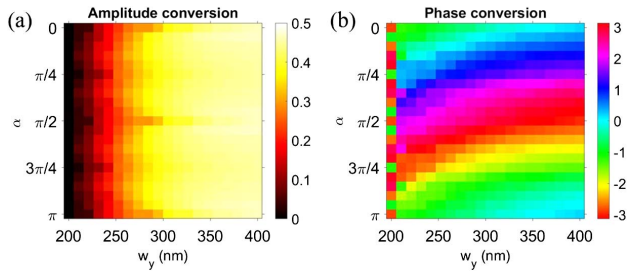

Fig. 6. (a) Amplitude conversion and (b) phase conversion under different w_y and orientation angle α when x is set at 200 nm and incident source is set at 1000 nm.

rication capacity. If w_x equals w_y, the Au block will show no birefringence. It means no LCP will be converted to RCP, which is consistent with the dark area in Fig. 6(a) where w_x is roughly equivalent to w_y.

Since the fabrication of a certain Au block has an error of about 10 nm, there is no point to pick (α, w_y) in Figs. 6(a) and 6(b) to match the exact amplitude and phase needed. Because later fabrication may deviate the selected point thus the desired complex modulation could not be achieved. To solve this issue, we conduct a parameter approximation. We select 10 points, which are 10 different w_y values, to round the continuous 0–1 amplitude to the nearest decimal, viz., from 0.1 to 1 in 10 discrete values. The continuous phase modulation is reached through the Pancharatnam–Berry phase by designing the orientation angle α of each individual gold nano-block, so there is no need to round the phase. The selected 10 different configurations are elaborated in Table 2 and are the same as in Fig. 1(c) in the red box.

Due to the fabrication limit, the maximum amplitude conversion we could obtain is 0.464. Therefore, a projection mapping from 0–1 to 0–0.464 is adopted to yield quasi 0–1 amplitude modulation. And the approximation mentioned above is taken to round the desired amplitude to the nearest one decimal. For example, if the desired amplitude conversion is 0.34, it will be rounded to 0.3 denoted as η_N, which after approximation could be written as $\eta_P = \eta_N \times 0.464 = 0.1392$. Next, we search over the simulated conversion map in Figs. 6(a) and 6(b) to find the appropriate parameters, including the length w_y and initial orientation α_0, on which the recomputed actual amplitude η_{ac} and phase ϕ_{ac} are based. Last, the relative error ξ is calculated as

$$\xi = \frac{|\eta_P e^{i\times(-1.129)} - \eta_{\mathrm{ac}} e^{i\times\phi_{\mathrm{ac}}}|}{0.464}, \tag{A13}$$

where −1.129 is the calibrated phase all configurations need to match at their initial orientation. In this example, after the actual amplitude conversion is computed as 0.1392, the length of the Au block w_y is determined as 230 nm. Then, the initial orientation α_0 is set at $-\frac{1}{60}\pi$, in order to offset the dynamic phase, which in other words is to make the initial phase conversion $\phi_{\mathrm{ac}} = -1.177$ as close to calibration −1.129 as possible. Under this configuration, we conduct the FDTD method to calculate the actual amplitude conversion η_{ac} and error ξ as detailed in Table 2.

APPENDIX B: PHASE-ONLY MODULATION COULD NOT ACHIEVE ZERO-ERROR

The electric field of an LG mode is detailed in Eq. (2). Here we simplify it as

$$\mathrm{LG}_p^l = A_{pl}(x,y) \cdot \exp[i\phi_{pl}(x,y)], \tag{B1}$$

where A_{pl} and ϕ_{pl} represent the amplitude and phase, respectively.

The ideal complex pattern containing exactly the desired LG modes could be written as

$$U = \sum_{p=0}^{\infty} \sum_{l=-\infty}^{\infty} \sigma_{pl} \cdot A_{pl}(x,y) \cdot \exp[i\phi_{pl}(x,y)], \tag{B2}$$

where σ_{pl} is a complex number.

If the metasurface could feature phase-only modulation, the complex pattern could be rewritten as $U = C \cdot \exp[i(\phi(x,y)]$, where C is a constant. The power is $P = |U|^2 = |C|^2$. Naturally, we will have

$$\sum_{p=0}^{\infty} \sum_{l=-\infty}^{\infty} \sum_{p'=0}^{\infty} \sum_{l'=-\infty}^{\infty} \sigma_{pl}\sigma_{p'l'} A_{pl} A_{p'l'} \cdot \exp\{i[\phi_{pl}(x,y) - \phi_{p'l'}(x,y)]\} = |C|^2. \tag{B3}$$

The above equation is not true for any arbitrary combination of more than two LG modes. Given the unimodular property [37], the Fourier basis, here the LG mode basis, should be either one or infinite in Eq. (B3). For finite LG modes, which are more than two LG modes but not infinite, Eq. (B3) is impossible. This is quite similar to Ref. [38], where the phase-only modulation for OAM combination is proved impossible.

APPENDIX C: LG MODE DECOMPOSITION

We use LG_p^l to denote the Laguerre-Gaussian mode with radial index p and azimuthal index l. The detailed expression is detailed in Eq. (2). The field of the LG mode LG_p^l is normalized throughout the paper, which means the highest amplitude is 1 for all the different modes.

Consider an electric field U, which could be decomposed into the combination of different LG modes as follows:

$$U = \sum_{p,l} C_p^l \cdot \mathrm{LG}_p^l, \tag{C1}$$

where C_p^l, a complex number, is the coefficient of the mode LG_p^l, which could be calculated as

$$C_p^l = \frac{\langle \mathrm{LG}_p^l, U\rangle}{\langle \mathrm{LG}_p^l, \mathrm{LG}_p^l\rangle} = \frac{\int \mathrm{LG}_p^{l*} \cdot U \mathrm{d}S}{\int \mathrm{LG}_p^{l*} \cdot \mathrm{LG}_p^l \mathrm{d}S}, \tag{C2}$$

where LG_p^{l*} is the conjugate of mode LG_p^l, and the integral area is the whole electric field S. The electric field U is normalized to ensure the highest amplitude is 1. Considering the different LG modes are also normalized, we have $\sum \mathrm{abs}(C_p^l) = 1$.

Since LG modes are orthogonal to each other, obviously we have

$$\frac{\int \mathrm{LG}_p^l * \cdot U \mathrm{d}S}{\int \mathrm{LG}_p^l * \cdot \mathrm{LG}_p^l \mathrm{d}S} = \begin{cases} 1, & p = p' \text{ and } l = l' \\ 0, & \text{otherwise} \end{cases}. \tag{C3}$$

Here we only consider the LG modes combination without deflection. It could give a basic idea of how the fabrication error will affect the final LG modes. However, if we introduce deflection into the decomposition, the results will cover a wide range of LG modes basis. It is similar to Ref. [39], where the OAM state is fixed but located away from the center, leading to a non-pure singular OAM in the spectrum. Such simplification could help us quantify the error and determine how much the error will influence our results.

For our metasurface M, detailed in Eq. (3), we first introduce the complex field U, which is equivalent with M but without deflection.

For the field U, the decomposition is

$$(C_p^l)_k = \frac{\int (\mathrm{LG}_p^l)_k^* \cdot U \mathrm{d}S}{\int (\mathrm{LG}_p^l)_k^* \cdot (\mathrm{LG}_p^l)_k \mathrm{d}S} = \sigma_k, \tag{C4}$$

where σ_k represents the weight assigned to mode $(\mathrm{LG}_p^l)_k$.

The relative intensity of each mode is written as

$$(I_p^l)_k \frac{\sigma_k^2}{\langle U, U \rangle} = \frac{\sigma_k^2}{\sum_i \langle \sigma_i (\mathrm{LG}_p^l)_i, \sigma_i (\mathrm{LG}_p^l)_i \rangle} = \frac{\sigma_k^2}{\sum_i \sigma_i^2}, \tag{C5}$$

where the sum of the intensity of all the modes is $\sum_k (I_p^l)_k = 1$. Due to conjugation, the phase information disappears in the intensity calculation step.

From Eq. (C1), we simplify the electric field as

$$U = A(x, y) \cdot \exp[i\phi(x, y)] = A_U \cdot \exp(i\phi_U). \tag{C6}$$

Given the assumption that the fabrication error of the width and length of the Au block is Gaussian distributed, it is reasonable to assume that it will lead to amplitude error being Gaussian distributed, which means the electric field of the fabricated metasurface is

$$U_{\mathrm{fab}} = [A(x, y) + t] \cdot \exp[i\phi(x, y)], \tag{C7}$$

where t is the amplitude of Gaussian distribution $N(\mu_a, \sigma_a^2)$. Note the mean μ_a and variance σ_a^2 of the amplitude error here

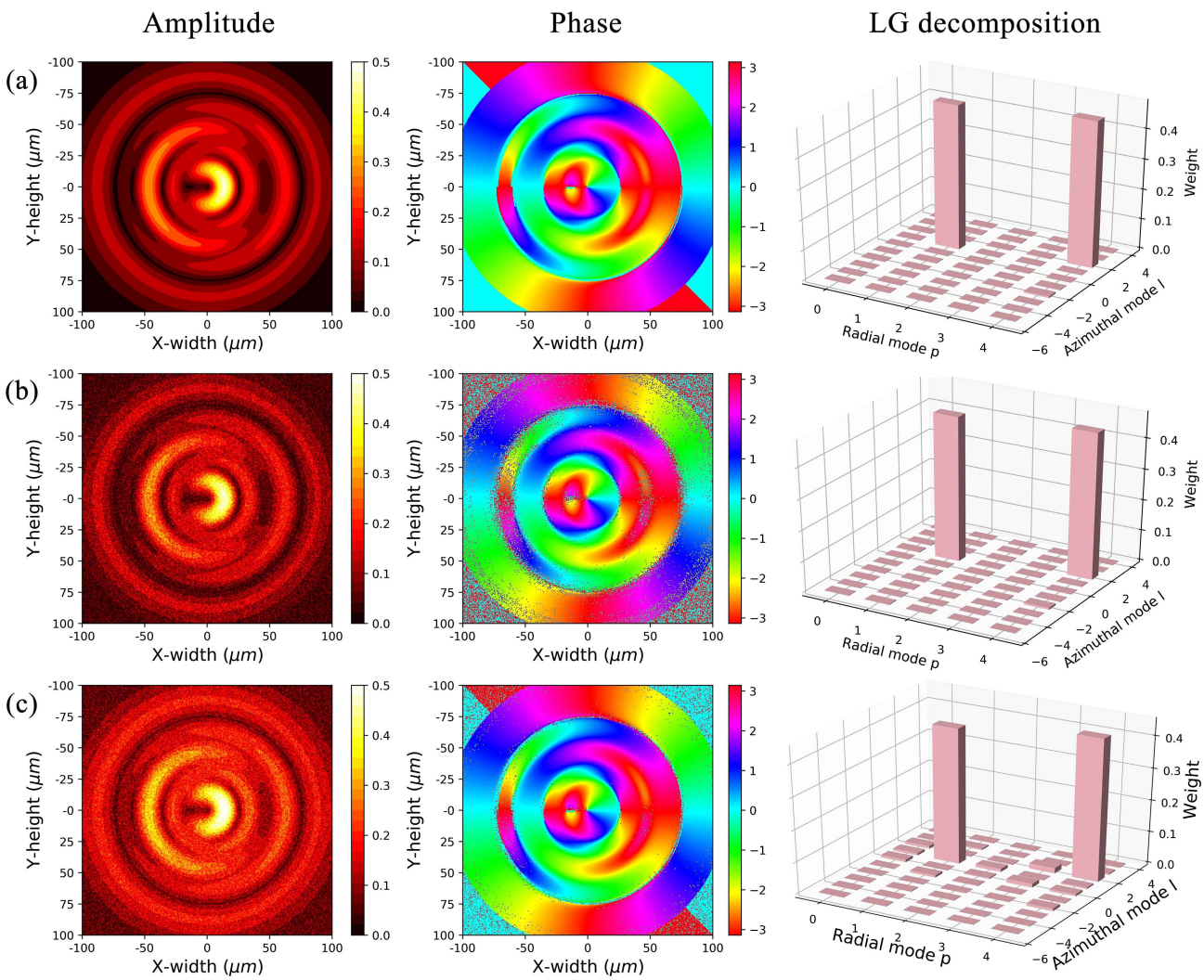

Fig. 7. First column: amplitude pattern. Second column: phase pattern. Third column: LG decomposition results. (a) Rounded complex pattern, featuring $\mathrm{LG}_4^2 : \mathrm{LG}_1^1 = 1:1$. (b) Complex pattern with a Gaussian noise $N(0{,}0.05^2)$ applied to the amplitude. (c) Complex pattern with a Gaussian noise $N(0.05{,}0.05^2)$ applied to the amplitude.

are different from the mean μ and variance σ^2 of fabrication error in Section 4.

Figure 7 reveals the complex pattern and LG decomposition results with regard to a metasurface, whose complex field is $U = \mathrm{LG}_4^2 + \mathrm{LG}_1^1$, with the weight ratio being $\mathrm{LG}_4^2 : \mathrm{LG}_1^1 = 1:1$ but without deflection compared to the metasurface field. The decomposition result is also shown in Fig. 2(e). Apparently, the error has little effect on our LG mode decomposition.

The deviation of width and length of the Au block will affect the amplitude and phase output. The error in this regard has been obtained through FDTD in Fig. 4. We assume the orientation does not change, so the Pancharatnam–Berry phase remains the same. The width and length deviation will affect the dynamic phase change, which is negligible if only considering ± 10 nm change. Therefore, the width and length deviation will only affect amplitude. Given that the fabrication machine is unbiased, it is intuitive to take the mean μ_a as 0. Under optimistic distribution in Table 2, the expectation of error ξ_3 ranges from 3.96% to 9.38%. It would be reasonable to choose a standard deviation σ_a in this scale. In Fig. 7, we assign σ_a a value of 0.05. The Gaussian noise $N(\mu_a, \sigma_a^2)$ is applied to the amplitude part of the combined LG mode pattern.

For demonstration, we write the LG mode as $\mathrm{LG}_p^l = A_p^l \cdot \exp(i\phi_p^l)$, where A_p^l and ϕ_p^l are both real numbers. The decomposition for the electric field after fabrication is

$$\begin{aligned}(C_p^l)_{\mathrm{fab}} &= \frac{\langle \mathrm{LG}_p^l, U_{\mathrm{fab}} \rangle}{\langle \mathrm{LG}_p^l, \mathrm{LG}_p^l \rangle} \rightarrow \int \mathrm{LG}_p^l \cdot U_{\mathrm{fab}} \mathrm{d}S, \\ &= \int A_p^l (A_U + t) \cdot \exp[i(\phi_U - \phi_p^l)] \mathrm{d}S \\ &= \int A_p^l A_U \cdot \exp[i(\phi_U - \phi_p^l)] \mathrm{d}S \\ &\quad + \int t \cdot A_p^l \cdot \exp[i(\phi_U - \phi_p^l)] \mathrm{d}S. \end{aligned} \tag{C8}$$

Since the normalization factor $\langle \mathrm{LG}_p^l, \mathrm{LG}_p^l \rangle$ is constant, we do not show it explicitly in Eq. (C8) for simplicity.

Given that t is a random variable, we take the expectation to get the final coefficient:

$$\begin{aligned}&(C_p^l)_{\mathrm{fab}} \leftarrow E[(C_p^l)_{\mathrm{fab}}] \\ &= \int A_p^l A_U \cdot \exp[i(\phi_U - \phi_p^l)] \mathrm{d}S \\ &\quad + \int t \cdot N(\mu_a, \sigma_a^2) \mathrm{d}t \int A_p^l \cdot \exp[i(\phi_U - \phi_p^l)] \mathrm{d}S \\ &= \int A_p^l A_U \cdot \exp[i(\phi_U - \phi_p^l)] \mathrm{d}S \\ &\quad + \mu_a \cdot \int A_p^l \cdot \exp[i(\phi_U - \phi_p^l)] \mathrm{d}S \\ &= C_p^l + \mu_a (C_p^l)_{\mathrm{phase}}, \end{aligned} \tag{C9}$$

where $(C_p^l)_{\mathrm{phase}}$ is the decomposition coefficient of the pure-phase modulation. From Eq. (C9), we could conclude that as long as the mean of amplitude error is 0, the noise term, which is the second term in Eq. (C9), could be waived. Even if the amplitude error has some bias, which means μ_a is not 0, the decomposition coefficient $(C_p^l)_{\mathrm{fab}}$ will be somewhere between complex modulation C_p^l and phase modulation $(C_p^l)_{\mathrm{phase}}$. If the bias is infinitely large (which is quite impossible in the sense), which means the amplitude error is large, the coefficient $(C_p^l)_{\mathrm{fab}}$ will degenerate into phase modulation $(C_p^l)_{\mathrm{phase}}$.

In order to quantify the deviation caused by the fabrication noise, here we set a criterion to judge the error in LG mode expansion.

The "error" in LG mode expansion here is defined as the sum of unwanted modes and the deviation from desired modes. Our desired coefficient vector of different LG modes is denoted as $\vec{\omega} = (\omega_0, \ldots, \omega_i, \ldots, \omega_n)$, while the coefficient after decomposition is $\vec{\sigma} = (\sigma_0, \ldots, \sigma_i, \ldots, \sigma_n)$, where ω_i and σ_i means the desired and decomposed coefficient for the ith mode, respectively, and n means all the modes desired.

The error could be calculated as

$$\epsilon = \sum_i \left| \frac{\omega_i}{\omega_0} - \frac{\sigma_i}{\sigma_0} \right|. \tag{C10}$$

The error could be interpreted as the deviation from the desired modes. We check whether the ratio of different modes is close to our predetermined ratio.

Here we define another term called efficiency, which is

$$\gamma = \sum_i \sigma_i. \tag{C11}$$

The efficiency is the sum of our desired modes. If a large ratio of power is split into unwanted modes, the metasurface will not generate desired modes even if the error ϵ is low.

Funding. National Natural Science Foundation of China (N_HKU712/16); Research Grants Council, University Grants Committee (CityU T42-103/16-N, E-HKU701/17, HKU 17200219, HKU 17209018, HKU C7047-16G).

Disclosures. The authors declare no conflicts of interest.

†These authors contributed equally to this work.

REFERENCES

1. W. N. Plick and M. Krenn, "Physical meaning of the radial index of Laguerre-Gauss beams," Phys. Rev. A **92**, 063841 (2015).
2. L. Allen, M. W. Beijersbergen, R. J. C. Spreeuw, and J. P. Woerdman, "Orbital angular momentum of light and the transformation of Laguerre-Gaussian laser modes," Phys. Rev. A **45**, 8185–8189 (1992).
3. A. Faßbender, J. Babocký, P. Dvořák, V. Křápek, and S. Linden, "Invited article: direct phase mapping of broadband Laguerre-Gaussian metasurfaces," APL Photonics **3**, 110803 (2018).
4. N. K. Fontaine, R. Ryf, H. Chen, D. T. Neilson, K. Kim, and J. Carpenter, "Laguerre-Gaussian mode sorter," Nat. Commun. **10**, 1865 (2019).
5. Y. Xiao, X. Tang, C. Wan, Y. Qin, H. Peng, C. Hu, and B. Qin, "Laguerre-Gaussian mode expansion for arbitrary optical fields using a subspace projection method," Opt. Lett. **44**, 1615–1618 (2019).
6. Y. Wang, X. Fang, Z. Kuang, H. Wang, D. Wei, Y. Liang, Q. Wang, T. Xu, Y. Zhang, and M. Xiao, "On-chip generation of broadband high-order Laguerre-Gaussian modes in a metasurface," Opt. Lett. **42**, 2463–2466 (2017).
7. G. Xie, H. Song, Z. Zhao, G. Milione, Y. Ren, C. Liu, R. Zhang, C. Bao, L. Li, Z. Wang, K. Pang, D. Starodubov, B. Lynn, M. Tur, and A. E.

Willner, "Using a complex optical orbital-angular-momentum spectrum to measure object parameters," Opt. Lett. **42**, 4482–4485 (2017).
8. M. P. Lavery, F. C. Speirits, S. M. Barnett, and M. J. Padgett, "Detection of a spinning object using light's orbital angular momentum," Science **341**, 537–540 (2013).
9. A. E. Willner, H. Huang, Y. Yan, Y. Ren, N. Ahmed, G. Xie, C. Bao, L. Li, Y. Cao, Z. Zhao, J. Wang, M. P. Lavery, M. Tur, S. Ramachandran, F. A. Molisch, N. Ashrafi, and S. Ashrafi, "Optical communications using orbital angular momentum beams," Adv. Opt. Photonics **7**, 66–106 (2015).
10. H. Ren, G. Briere, X. Fang, P. Ni, R. Sawant, S. Héron, S. Chenot, S. Vézian, B. Damilano, V. Brändli, S. A. Maier, and P. Genevet, "Metasurface orbital angular momentum holography," Nat. Commun. **10**, 2986 (2019).
11. G. Gbur and R. K. Tyson, "Vortex beam propagation through atmospheric turbulence and topological charge conservation," J. Opt. Soc. Am. A **25**, 225–230 (2008).
12. F. Yue, D. Wen, C. Zhang, B. D. Gerardot, W. Wang, S. Zhang, and X. Chen, "Multichannel polarization-controllable superpositions of orbital angular momentum states," Adv. Mater. **29**, 1603838 (2017).
13. S. Li, X. Li, L. Zhang, G. Wang, L. Zhang, M. Liu, C. Zeng, L. Wang, Q. Sun, W. Zhao, and W. Zhang, "Efficient optical angular momentum manipulation for compact multiplexing and demultiplexing using a dielectric metasurface," Adv. Opt. Mater. **8**, 1901666 (2020).
14. E. Karimi, R. Boyd, P. De La Hoz, H. De Guise, J. Řeháček, Z. Hradil, A. Aiello, G. Leuchs, and L. L. Sánchez-Soto, "Radial quantum number of Laguerre-Gauss modes," Phys. Rev. A **89**, 063813 (2014).
15. K. Sueda, G. Miyaji, N. Miyanaga, and M. Nakatsuka, "Laguerre-Gaussian beam generated with a multilevel spiral phase plate for high intensity laser pulses," Opt. Express **12**, 3548–3553 (2004).
16. H. Sztul and R. Alfano, "Double-slit interference with Laguerre-Gaussian beams," Opt. Lett. **31**, 999–1001 (2006).
17. H. Luo, Z. Ren, W. Shu, and S. Wen, "Reversed propagation dynamics of Laguerre-Gaussian beams in left-handed materials," Phys. Rev. A **77**, 023812 (2008).
18. S. Khonina, V. Kotlyar, R. Skidanov, V. Soifer, P. Laakkonen, and J. Turunen, "Gauss-Laguerre modes with different indices in prescribed diffraction orders of a diffractive phase element," Opt. Commun. **175**, 301–308 (2000).
19. C. Wan, J. Chen, and Q. Zhan, "Tailoring optical orbital angular momentum spectrum with spiral complex field modulation," Opt. Express **25**, 15108–15117 (2017).
20. M. Rafayelyan and E. Brasselet, "Laguerre Gaussian modal *Q*-plates," Opt. Lett. **42**, 1966–1969 (2017).
21. M. Rafayelyan, T. Gertus, and E. Brasselet, "Laguerre-Gaussian quasi-modal *Q*-plates from nanostructured glasses," Appl. Phys. Lett. **110**, 261108 (2017).
22. N. Yu, P. Genevet, M. A. Kats, F. Aieta, J.-P. Tetienne, F. Capasso, and Z. Gaburro, "Light propagation with phase discontinuities: generalized laws of reflection and refraction," Science **334**, 333–337 (2011).
23. X. Ni, N. K. Emani, A. V. Kildishev, A. Boltasseva, and V. M. Shalaev, "Broadband light bending with plasmonic nanoantennas," Science **335**, 427 (2012).
24. X. Chen, L. Huang, H. Muhlenbernd, G. Li, B. Bai, Q. Tan, G. Jin, C.-W. Qiu, S. Zhang, and T. Zentgraf, "Dual-polarity plasmonic metalens for visible light," Nat. Commun. **3**, 1198 (2012).
25. D. Lin, P. Fan, E. Hasman, and M. L. Brongersma, "Dielectric gradient metasurface optical elements," Science **345**, 298–302 (2014).
26. B. Sang, Y. Ke, J. Wu, H. Luo, W. Shu, and S. Wen, "Generation of pure Laguerre-Gaussian vector beams on the higher-order Poincaré sphere by hollow Gaussian beams through dielectric metasurfaces," Opt. Commun. **439**, 27–33 (2019).
27. Z. Bomzon, G. Biener, V. Kleiner, and E. Hasman, "Space-variant Pancharatnam-Berry phase optical elements with computer-generated subwavelength gratings," Opt. Lett. **27**, 1141–1143 (2002).
28. M. Kang, T. Feng, H.-T. Wang, and J. Li, "Wave front engineering from an array of thin aperture antennas," Opt. Express **20**, 15882–15890 (2012).
29. L. Huang, X. Chen, H. Mühlenbernd, G. Li, B. Bai, Q. Tan, G. Jin, T. Zentgraf, and S. Zhang, "Dispersionless phase discontinuities for controlling light propagation," Nano Lett. **12**, 5750–5755 (2012).
30. G. Zheng, H. Mühlenbernd, M. Kenney, G. Li, T. Zentgraf, and S. Zhang, "Metasurface holograms reaching 80% efficiency," Nat. Nanotechnol. **10**, 308–312 (2015).
31. H.-T. Chen, A. J. Taylor, and N. Yu, "A review of metasurfaces: physics and applications," Rep. Prog. Phys. **79**, 076401 (2016).
32. A. C. Overvig, S. Shrestha, S. C. Malek, M. Lu, A. Stein, C. Zheng, and N. Yu, "Dielectric metasurfaces for complete and independent control of the optical amplitude and phase," Light Sci. Appl. **8**, 92 (2019).
33. G. Xie, Y. Ren, Y. Yan, H. Huang, N. Ahmed, L. Li, Z. Zhao, C. Bao, M. Tur, S. Ashrafi, and A. E. Willner, "Experimental demonstration of a 200-Gbit/s free-space optical link by multiplexing Laguerre-Gaussian beams with different radial indices," Opt. Lett. **41**, 3447–3450 (2016).
34. R. Borghi, F. Gori, and M. Santarsiero, "Optimization of Laguerre-Gauss truncated series," Opt. Commun. **125**, 197–203 (1996).
35. L. Novotny and B. Hecht, *Principles of Nano-Optics* (Cambridge University, 2012).
36. Y. Fazea and A. Amphawan, "40 Gbit/s MDM-WDM Laguerre-Gaussian mode with equalization for multimode fiber in access networks," J. Opt. Commun. **39**, 175–184 (2018).
37. B. Picinbono, "On instantaneous amplitude and phase of signals," IEEE Trans. Signal Process. **45**, 552–560 (1997).
38. J. Lin, X.-C. Yuan, S. H. Tao, and R. E. Burge, "Collinear superposition of multiple helical beams generated by a single azimuthally modulated phase-only element," Opt. Lett. **30**, 3266–3268 (2005).
39. G. Molina-Terriza, J. P. Torres, and L. Torner, "Management of the angular momentum of light: preparation of photons in multidimensional vector states of angular momentum," Phys. Rev. Lett. **88**, 013601 (2001).